

1 **Uncertainty in 21<sup>st</sup> Century Projections of the Atlantic Meridional Overturning**  
2 **Circulation in CMIP3 and CMIP5 models**

3

4 A. Reintges (corresponding author), T. Martin, M. Latif

5 GEOMAR Helmholtz Centre for Ocean Research Kiel

6 Düsternbrooker Weg 20, 24105 Kiel, Kiel, Germany

7 e-mail: areintges@geomar.de

8 telephone: +49 431 600-4007

9 fax: +49 431 600-4052

10

11 N. S. Keenlyside

12 Geophysical Institute and Bjerknes Centre, University of Bergen

13 Allégaten 70, 5020 Bergen, Norway

14

15

16

17

18

19

20

21

22

23 NOTE: This is a post-peer-review, pre-copyedit version of an article published in Climate  
24 Dynamics. The final authenticated version is available online at:  
25 <https://link.springer.com/article/10.1007/s00382-016-3180-x>

26 Please cite as Reintges, A., Martin, T., Latif, M. and Keenlyside, N. S. (2017) Uncertainty in  
27 twenty-first century projections of the Atlantic Meridional Overturning Circulation in CMIP3  
28 and CMIP5 models. Climate Dynamics 49:1495-1511. doi:10.1007/s00382-016-3180-x

29 **Uncertainty in 21<sup>st</sup> Century Projections of the Atlantic Meridional Overturning**  
30 **Circulation in CMIP3 and CMIP5 models**

31 Annika Reintges, Thomas Martin, Mojib Latif and Noel S. Keenlyside

32 Abstract

33 Uncertainty in the strength of the Atlantic Meridional Overturning Circulation (AMOC) is  
34 analyzed in the Coupled Model Intercomparison Phase 3 (CMIP3) and Phase 5 (CMIP5)  
35 projections for the 21<sup>st</sup> century; and the different sources of uncertainty (scenario, internal and  
36 model) are quantified. Although the uncertainty in future projections of the AMOC index at  
37 30°N is larger in CMIP5 than in CMIP3, the signal-to-noise ratio is comparable during the  
38 second half of the century and even larger in CMIP5 during the first half. This is due to a  
39 stronger AMOC reduction in CMIP5. At lead times longer than a few decades, model  
40 uncertainty dominates uncertainty in future projections of AMOC strength in both the CMIP3  
41 and CMIP5 model ensembles. Internal variability significantly contributes only during the first  
42 few decades, while scenario uncertainty is relatively small at all lead times. Model uncertainty  
43 in future changes in AMOC strength arises mostly from uncertainty in density, as uncertainty  
44 arising from wind stress (Ekman transport) is negligible. Finally, the uncertainty in changes in  
45 the density originates mostly from the simulation of salinity, rather than temperature. High-  
46 latitude freshwater flux and the subpolar gyre projections were also analyzed, because these  
47 quantities are thought to play an important role for the future AMOC. The freshwater input in  
48 high latitudes is projected to increase and the subpolar gyre is projected to weaken. Both the  
49 freshening and the gyre weakening likely influence the AMOC by causing anomalous salinity  
50 advection into the regions of deep water formation. While the high model uncertainty in both  
51 parameters may explain the uncertainty in the AMOC projection, deeper insight into the  
52 mechanisms for AMOC is required to reach a more quantitative conclusion.

53 Keywords: Atlantic Meridional Overturning Circulation (AMOC), North Atlantic ocean,  
54 uncertainty, climate projections

55

## 56 **1. Introduction**

57 The AMOC (Ganachaud and Wunsch 2003; Srokosz et al. 2012) is characterized by a  
58 northward flow of warm, salty water in the upper layers of the Atlantic, and a southward return  
59 flow of colder water in the deep Atlantic (Dickson and Brown 1994). It transports a substantial  
60 amount of heat from the tropics and Southern Hemisphere toward the North Atlantic, where the  
61 heat is then transferred to the atmosphere. The mild climate of Northern Europe is in part a  
62 consequence of this heat supply. Changes in the AMOC are thought to have a profound impact  
63 on many aspects of the global climate system. For example, the Atlantic Multidecadal  
64 Oscillation or Variability (AMO/V), a coherent pattern of multidecadal variability in surface  
65 temperature centered on the North Atlantic Ocean, is linked to the AMOC in climate models  
66 (Knight et al. 2005; Zhang and Delworth 2006). Further aspects that are hypothesized to be  
67 related to the AMOC are: observed decadal variability in the air-sea heat exchange over the  
68 North Atlantic (Gulev et al. 2013), continental summertime climate of both North America and  
69 western Europe (Sutton and Hodson 2005), Atlantic hurricane activity, Sahel rainfall and the  
70 Indian Summer Monsoon (Zhang and Delworth 2006).

71 Direct measurements of AMOC strength from the RAPID-MOCHA array at 26.5°N reveal a  
72 decline since 2004 (McCarthy et al. 2012, Smeed et al. 2014): During 2008-2012 the AMOC  
73 was 2.7 Sv ( $1 \text{ Sv} = 10^6 \text{ m}^3/\text{s}$ ) weaker than during 2004-2008. Because of the relatively short  
74 observational record it is unclear whether this decline is just a short-term fluctuation or part of  
75 a long-term trend. However, records show that density in the Labrador Sea began to fall in the  
76 late 1990s, and this may suggest more persistent AMOC weakening (Robson et al. 2014).

77 Roberts et al. (2014) suggest that this decline could be due to internal variability. However,  
78 they also stress that the CMIP5 models generally underestimate the interannual variability of  
79 the AMOC. This may be also the case at decadal timescales due to salinity biases, as recently  
80 discussed by Park et al. (2016).

81 How will the AMOC evolve during the next decades and the whole 21<sup>st</sup> century? Future changes  
82 in the AMOC will result from both internal and external processes of the climate system. On  
83 the one hand, in control integrations with fixed external forcing many climate models simulate  
84 strong internal AMOC variability on decadal to multi-decadal and even centennial timescales  
85 (e.g., Danabasoglu 2008; Latif et al. 2004; Knight et al. 2005; Park and Latif 2008; Delworth  
86 and Zeng 2012; see Latif and Keenlyside 2011 for a review). On the other hand, external forcing  
87 such as anthropogenic emissions of long-lived greenhouse gases (GHGs) driving global  
88 warming may also influence the future AMOC, as has been shown in numerous modeling  
89 studies. The internal decadal to centennial AMOC variability will superimpose and hinder  
90 detection of a potential anthropogenic AMOC signal, which evolves on similar timescales.

91 A wide variety of mechanisms have been put forward for how global warming will influence  
92 AMOC. Global warming in response to enhanced atmospheric GHG concentrations will be  
93 accompanied by changes in the vertical temperature and salinity profiles in the ocean. The  
94 meridional structure of these changes will affect the meridional oceanic density contrast, which  
95 has been suggested to be correlated with the AMOC strength (e.g., Thorpe et al. 2001).  
96 Additionally to the importance of these processes, a large number of theoretical and modeling  
97 studies pointed out the control of the AMOC by a number of internal ocean processes (as  
98 reviewed by Kuhlbrodt et al., 2007). Delworth et al. (1993) suggested an interdecadal  
99 oscillation caused by the interaction between the AMOC and the horizontal gyre circulation.  
100 The influence of the subpolar gyre on the AMOC was supported by a multi-model study of Ba  
101 et al. (2014). Further, a remote influx at the depth of the overturning, due to changes in the

102 Southern Ocean wind stress and Antarctic Bottom Water (AABW) formation, might counteract  
103 the effect of changes in the meridional density gradient (de Boer et al. 2010). Shakespeare and  
104 Hogg (2012) found that the AMOC scales linearly with both the Southern Ocean wind stress  
105 and northern buoyancy flux. Gnanadesikan (1999) pointed out that the difference between  
106 northern sinking and upwelling in the Southern Ocean are balanced by changes in the low-  
107 latitude isopycnal depth. The rate of sinking in the north depends on the parameterization of  
108 vertical mixing. Sijp et al. (2006) derived the importance of isopycnal mixing in models,  
109 because it does not require a strong vertical instability. They argue that buoyancy-driven  
110 convection overestimates the sensitivity of deep water production against surface freshwater  
111 fluxes. The temporal and spatial interactions of all these processes determine the mean state,  
112 the internal variability and the externally caused changes of the AMOC intensity. Finally, the  
113 relative importance of these processes is unknown under changing climate conditions, and  
114 might be different from the importance of the processes that determine the mean state in climate  
115 model projections. Thus there are major uncertainties in how AMOC will respond to global  
116 warming.

117 Climate models generally predict a weakening of the AMOC during the 21<sup>st</sup> century when  
118 forced by enhanced levels of GHG concentrations, but large uncertainties exist (e.g., Schmittner  
119 et al. 2005). This uncertainty can be conceptually decomposed into three components (Hawkins  
120 and Sutton 2009, Hawkins and Sutton 2011): First, the future GHG emissions are unknown.  
121 The climate models are therefore run under different GHG scenarios, leading to the so-called  
122 scenario uncertainty. Second, a large uncertainty exists, even under identical GHG forcing  
123 (Schmittner et al. 2005). One reason for this uncertainty is internal stochastically driven AMOC  
124 fluctuations (e.g., Park and Latif 2012, Mecking et al. 2014). This kind of uncertainty is called  
125 internal variability. Third, there is uncertainty arising from model systematic error that is called  
126 model uncertainty, also sometimes termed response uncertainty. Model uncertainty might

127 originate from the ocean, the atmospheric or the sea ice components of the coupled models,  
128 since all three influence the surface fluxes of heat, freshwater and momentum that drive the  
129 AMOC. For example, the large mean biases in the North Atlantic found in the most climate  
130 models (Wang et al. 2014) lead to errors in the northward path of saline waters, potentially  
131 affecting internal variability and the model response to enhanced GHG concentrations.

132 The main purpose of this study is to investigate the consistency between the CMIP models with  
133 regard to projecting 21<sup>st</sup> century GHG-forced AMOC change and to identify the origin of  
134 uncertainties. As the complex processes controlling AMOC are poorly understood, a full  
135 mechanistic understanding of future projections in AMOC remains a major challenge in climate  
136 research and is beyond the scope of this paper. The focus of this paper is rather to examine a  
137 few key variables that have been identified to be of relevance for the AMOC. We follow the  
138 methodology outlined by Hawkins and Sutton (2009) and quantify as function of lead time the  
139 three individual contributions – scenario, internal, and model – to the total AMOC projection  
140 uncertainty. We show that, in both the CMIP3 and CMIP5 model ensembles, model uncertainty  
141 dominates AMOC projections for the 21<sup>st</sup> century at lead times beyond a few decades. This  
142 paper is organized as follows. In Section 2, we describe the data and the methodology used in  
143 this study. We present the results of the AMOC projection uncertainty analysis in Section 3.  
144 The results are summarized in Section 4.

## 145 **2. Data and methodology**

### 146 *Data*

147 We have used climate model simulations from the World Climate Research Programme's  
148 (WCRP's) Coupled Model Intercomparison Project phase 3 (CMIP3; Table 1) (Meehl et al.  
149 2007a) and phase 5 (CMIP5; Table 2) (Taylor et al. 2012). The multi-model datasets are  
150 provided by the Program for Climate Model Diagnosis and Intercomparison (PCMDI). From

151 CMIP3 we used the 20C3M data for the 20<sup>th</sup> century and the IPCC SRES scenarios A1B, A2,  
152 and B1 for the 21<sup>st</sup> century. The scenario B1 comprises the weakest, A1B a moderate, and A2  
153 the strongest radiative forcing. For the CMIP5 analysis, we used the ‘historical’ data  
154 representing the 20<sup>th</sup> century and the RCP4.5 and RCP8.5 scenarios for the 21<sup>st</sup> century. These  
155 two scenarios are core experiments of CMIP5, and thus were performed with virtually all  
156 participating models. The scenario with higher radiative forcing is RCP8.5. Combining the  
157 20<sup>th</sup>- and the 21<sup>st</sup>-century scenarios our analysis covers the period 1850-2100. The CMIP  
158 models provide the depth profile of the meridional overturning streamfunction in the Atlantic,  
159 defined in z-coordinates and as function of latitude. From this variable we also computed the  
160 indices of the AMOC strength by taking the maximum in the vertical for a given latitude. This  
161 is a common measure of the AMOC strength. In the CMIP3 ensemble, the mean depth of the  
162 overturning streamfunction maximum at 30°N during the years 1970-2000 is 1,115 m with an  
163 inter-model standard deviation of 519 m and in the CMIP5 ensemble, 1,036 m with an inter-  
164 model standard deviation of 140 m. These numbers seem to be reasonable when compared to  
165 the observed profile at 26°N which also depicts a maximum at roughly 1,100 m (Smeed et al.  
166 2014). For our analysis we use the latitudes 30°N and 48°N, because in most models 30°N  
167 matches the center of the overturning cell quite well, whereas 48°N is a location with large  
168 variability. Furthermore, zonal mean salinity and potential temperature profiles are analyzed in  
169 this study. These were also used to calculate density changes. We also investigate the Arctic  
170 and North Atlantic freshwater fluxes (WFO) from 0°-90°N integrated over different areas.  
171 WFO includes the effects of evaporation, precipitation, river runoff, and sea ice changes.  
172 Finally, we compute the uncertainties also for the subpolar gyre index, which is derived from  
173 the barotropic streamfunction.

174 For most of the variables, we perform most of our analysis separately on both CMIP3 and  
175 CMIP5 data. The total number of models in the CMIP3 database is smaller than that of CMIP5

176 (Tables 1 and 2). Of course, the models are not entirely independent of each other; some models  
177 originate from the same modeling center and some share the same model components (Masson  
178 and Knutti 2011). Therefore, the model uncertainty derived from the model ensemble used here  
179 could be biased. To test this, we repeated the analyses with a smaller ensemble by removing  
180 those models that have a setting too close to another model or behave too similar regarding one  
181 or more variables. Our main findings remained qualitatively unchanged in these tests. Finally,  
182 one should note that the forcing used in the CMIP3 and CMIP5 integrations is similar but not  
183 identical; this is discussed below in the result section.

#### 184 *Statistical method*

185 Uncertainty is a term used in different fields. In this study, uncertainty reflects the spread  
186 between ensemble members within the CMIP projection of future climate. The CMIP data offer  
187 a wide range of results for historic simulations and future climate projections. As the true path  
188 of AMOC strength is unknown, it is difficult to evaluate the quality of the model-based future  
189 projections. To define uncertainty we derive variances from inter-simulation differences. Total  
190 uncertainty may not be decomposed into a linear combination of individual sources of  
191 uncertainty, as cross terms may exist (i.e., variance of one component might depend on one of  
192 the other factors). For example, the sensitivity to a specified forcing scenario and the internal  
193 variability could be related and be model-dependent. However, here we are not interested in the  
194 uncertainty of individual model projections, but only in integral quantities computed over the  
195 complete model ensemble. Furthermore, we analyzed the cross terms and found them to be  
196 sufficiently small not to impact the major conclusions of this work, and thus they will be  
197 neglected in the remainder of the analysis.

198 For the quantification of the three sources of uncertainty we basically follow the approach  
199 suggested by Hawkins and Sutton (2009), although we adapted the method for calculating the  
200 internal variability. A more complete framework has been proposed, but it was shown to give



201 similar results when analyzing CMIP3 models (Yip et al. 2011). For a given scalar variable of  
 202 our analysis (e.g. AMOC strength or density at a fixed position) we define the term model  
 203 projections  $X(m,s,t)$  as the climate realizations dependent on time,  $t$ , and obtained from various  
 204 CMIP models,  $m$ , and different 21<sup>st</sup> century forcing scenarios,  $s$ . The projections  $X(m,s,t)$  are  
 205 split into a long-term variability component, representing the response to external forcing  
 206  $X_f(m,s,t)$ , and a short-term residual  $\varepsilon(m,s,t)$ , representing internal fluctuations:

$$207 \quad X(m,s,t) = X_f(m,s,t) + \varepsilon(m,s,t) \quad (1).$$

208 A model response to external forcing is typically computed as the mean across a large ensemble  
 209 of experiments performed with that model prescribing identical external forcing but started  
 210 from different initial conditions. In the absence of such data we estimate the external forced  
 211 AMOC component,  $X_f(m,s,t)$ , by a 4<sup>th</sup> order polynomial fit computed over the full time series.  
 212 A 4<sup>th</sup>-order polynomial is chosen as it captures the non-linear response of AMOC to external  
 213 forcing that includes the reduced weakening of the AMOC at the end of the 21<sup>st</sup> century found  
 214 in several models. Our main conclusions remain insensitive to this choice, as shown by  
 215 repeating the uncertainty analysis of the AMOC index at 30°N from the CMIP5 ensemble with  
 216 polynomial orders from 2, 3, and 5 (see supplementary material).

217 Then, from the long-term fit  $X_f(m,s,t)$  we calculate a long-term anomaly  $x_f(m,s,t)$  relative to the  
 218 initial value  $i(m,s)$ , which is the average over the years 1970 to 2000:

$$219 \quad X_f(m,s,t) = i(m,s) + x_f(m,s,t) \quad (2).$$

220 Three sources of uncertainty are distinguished. The calculation of these components involves  
 221 taking the variance over the respective component. In our equations, we use a variance operator  
 222 defined as follows:

$$223 \quad VAR_d(p) = \frac{1}{N_d - 1} \sum_d \left( p - \frac{1}{N_d} \sum_d p \right)^2 \quad (3).$$

224 Here,  $p$  is any parameter for which the variance is computed in the dimension  $d$ .

225 The first source of uncertainty is the internal variability and defined as

$$226 \quad I = \frac{1}{N_s} \sum_s \frac{1}{N_m} \sum_m VAR_t(\varepsilon(m, s, t)) \quad (4).$$

227  $N_s$  and  $N_m$  are the numbers of scenarios and models, respectively. Internal variability is  
228 represented by the variance of the residual  $\varepsilon(m, s, t)$  over time, averaged over all models and all  
229 scenarios. Therefore, internal variability is given as one value.

230 The second source of uncertainty is the model uncertainty and defined as

$$231 \quad M(t) = \frac{1}{N_s} \sum_s VAR_m(x_f(m, s, t)) \quad (5).$$

232 It represents the spread between the different model realizations. Here, we take the variance of  
233 the long-term anomaly  $x_f(m, s, t)$  over the model dimension  $m$ , and then average over the different  
234 scenarios. According to our definition the internal variability includes only frequencies on inter-  
235 annual or decadal timescales. Since the AMOC exhibits long-term variability (e.g. the Atlantic  
236 Multidecadal Variability, AMV), which cannot be completely filtered out by the polynomial  
237 fit, the model uncertainty contains also some uncertainty due to internal variability.

238 The third source of uncertainty is the scenario uncertainty and defined as

$$239 \quad S(t) = VAR_s \left( \frac{1}{N_m} \sum_m x_f(m, s, t) \right) \quad (6).$$

240 It represents the spread of the long-term anomaly  $x_f(m, s, t)$ , averaged over all models for each  
241 scenario. The estimate of the total uncertainty  $T(t)$  is defined as the sum of the internal, model  
242 and scenario uncertainty. Finally, we calculated the signal-to-noise ratio  $SNR(t)$  with a two-  
243 sided confidence level  $c$ :

244 
$$SNR(t) = \frac{G(t)}{q_{\frac{c}{2}} \sqrt{T(t)}} \quad (7).$$

245 Here  $q_{\frac{c}{2}}$  is the  $\frac{c}{2}$ <sup>th</sup> quantile of the standard normal distribution. In this analysis, a confidence  
 246 level of 90% is used.  $G(t)$  is the mean signal

247 
$$G(t) = \frac{1}{N_s} \sum_s \frac{1}{N_m} \sum_m x_f(m, s, t) \quad (8)$$

248 which is estimated from the averaged model fit  $x_f$  considering all models and scenarios. A  
 249 signal-to-noise ratio  $SNR(t)$  larger than unity indicates that the mean climate signal  $G(t)$  exceeds  
 250 the amplitude of the noise and is therefore detectable. The uncertainty analysis below is based  
 251 on decadal means.

### 252 **3. Results**

#### 253 *AMOC*

254 The ensemble-mean of the late 20<sup>th</sup> century (1970-2000) Atlantic meridional overturning  
 255 streamfunction depicts a distinct maximum just below 1000 m in the region 30°N-45°N in both  
 256 the CMIP3 (Fig. 1a) and CMIP5 (Fig. 1d) model ensemble. The North Atlantic Deep Water  
 257 (NADW) cell reaches down to roughly 3000 m, which is shallower than what observations  
 258 suggest (McCarthy et al. 2012). We note, however, that the vertical extent of the cell varies  
 259 from model to model. The overall structure of the ensemble-mean is rather similar in the two  
 260 CMIP ensembles, but the mean strength of the overturning is considerably stronger in the  
 261 CMIP5 ensemble. The vertical maximum at 26°N is close to 19 Sv in the CMIP5 ensemble, as  
 262 opposed to 16 Sv in the CMIP3 ensemble. These numbers are closer to the observations  
 263 obtained from the RAPID array at 26°N, indicating AMOC strength of about 17.5 Sv during  
 264 the years 2004-2012 (Smeed et al. 2014). Decadal variability, however, may be large.  
 265 Furthermore, it must be noted that the spread among the models is huge and for the vertical

266 maximum at 26°N the models provide a range of 12.1 - 29.7 Sv in CMIP5 and 6.6 – 27.4 Sv in  
267 CMIP3. The ensemble-mean AABW cell, which is located below the NADW cell, is rather  
268 similar in both ensembles.

269 The ensemble-mean projected change in the Atlantic meridional overturning streamfunction for  
270 the end of the 21<sup>st</sup> century (2090-2100 relative to 1970-2000) is shown in Fig. 1b and 1e. A  
271 clear weakening of the NADW cell is seen in both ensembles, with the strongest change in the  
272 streamfunction near 40°N, while there is a slight strengthening of the AABW cell. The spatial  
273 pattern of the change is rather similar, but the magnitude is considerably stronger in the CMIP5  
274 ensemble. In both ensembles, the maximum reduction occurs below the absolute maximum of  
275 the ensemble-mean streamfunction, which results in a shallower NADW cell. We note that  
276 although the radiative forcing is roughly comparable in the two ensembles, it is not identical.  
277 For example, the changes in global annual-mean surface air temperature by the year 2100  
278 depending on the scenario are: in CMIP3 1.8°C (B1), 2.8°C (A1B), 3.6°C (A2) relative to 1980-  
279 1999 (Meehl et al. 2007b); and in CMIP5 1.9°C (RCP4.5), 4.1°C (RCP8.5) relative to 1986-  
280 2005 (Collins et al. 20013). The relative change of the overturning is comparable and amounts  
281 to about a 25-30% reduction by the end of the 21<sup>st</sup> century. The stronger absolute weakening in  
282 the CMIP5 ensemble causes a larger signal-to-noise ratio in the CMIP5 ensemble with a  
283 maximum of about 1.5 (Fig. 1f) as opposed to about 1 in the CMIP3 ensemble (Fig. 1c). A  
284 signal-to-noise ratio of unity denotes the significance limit with 90%-confidence. Thus, a value  
285 of 1.5 is indicative of a highly significant and detectable change.

286 In the following, we take the maxima of the streamfunction at 30°N and 48°N as indices for the  
287 AMOC strength. The 30°N index is close to the center of the overturning cell and also is a good  
288 indicator for a large meridional scale of the cell. Additionally, we select an AMOC index at  
289 48°N that is close to the northern edge of the overturning cell and displays higher variability  
290 than the index at 30°N. We show the individual projections at 30°N for both CMIP3 (Fig. 2a)

291 and CMIP5 (Fig. 2d), for each model and for each scenario, with a 10-year running mean  
292 applied to aid visualization (but all uncertainty analysis is performed on decadal means). A  
293 large spread is obvious in the long-term AMOC projections at 30°N in the CMIP3 and CMIP5  
294 ensembles. In both ensembles, the largest contribution to the total uncertainty is related to the  
295 model differences (blue) at almost all lead times (Fig. 2b, 2e); while the contribution from the  
296 internal variability (red) is rather small at all lead times. Although climate models may  
297 underestimate the interannual variability of the AMOC (Roberts et al. 2014), model uncertainty  
298 would still dominate by far even if the internal variability component was twice as large as  
299 estimated here. Similarly, model uncertainty dominates for any reasonable choice of  
300 polynomial order used to identify the forced component (see supplementary material). By 2100,  
301 the contribution of scenario uncertainty (green) is substantial (about 20%) in the CMIP5  
302 ensemble, but is rather small in the CMIP3 ensemble. This may be partly related to the larger  
303 range of radiative forcing and to larger model sensitivity in CMIP5. Independently of this, the  
304 main conclusion is unchanged as we move from CMIP3 to CMIP5: the model uncertainty is by  
305 far the largest contribution to the total uncertainty in the AMOC projections for the 21<sup>st</sup> century  
306 at lead times of several decades and beyond. Both CMIP ensembles yield a relatively large  
307 signal-to-noise ratio for the AMOC change at 30°N (red line in Fig. 2c and 2f) at lead times  
308 beyond a few decades. The signal-to-noise ratio tends to diminish at longer lead times. This  
309 reflects the dominance of the model uncertainty compared to the projected AMOC reduction.  
310 The signal-to-noise ratio is generally larger at 30°N than at 48°N (blue line in Fig. 2c and 2f),  
311 which indicates a greater detectability of an anthropogenic signal in the subtropics compared to  
312 the mid-latitudes.

313 Although geostrophic transport dominates the time-mean AMOC, both geostrophic and Ekman  
314 transports are important in explaining the AMOC variability. We derived the Ekman  
315 contribution to the AMOC model uncertainty at 30°N from the wind stress curl field (Visbeck

316 et al. 2003). The Ekman component of model uncertainty is shown together with the remaining  
317 model uncertainty and the other two uncertainty sources in Fig. 3. The Ekman contribution  
318 (yellow) is rather small and becomes comparable to the AMOC uncertainty due to the internal  
319 variability by the end of the 21<sup>st</sup> century. The Ekman uncertainty is thus, in both model  
320 ensembles, only a marginal contributor to the total AMOC projection uncertainty.

321 As scenario uncertainty plays only a minor role compared to model uncertainty, we will focus  
322 on only one scenario per model ensemble during all following analyses. We choose scenarios  
323 with a moderate radiative forcing: SRES A1B for CMIP3 and RCP4.5 for CMIP5. One should  
324 keep in mind that the global-mean surface air temperature change by the year 2100 is larger in  
325 A1B (2.8°C relative to 1980-1999) than in RCP4.5 (1.9°C relative to 1986-2005).

326 We benchmark the relationships of the AMOC to several parameters that have been previously  
327 identified as relevant, for both CMIP3 and CMIP5 ensembles as follows: Table 3 lists  
328 correlations computed across the model ensembles between the AMOC index at 30°N and these  
329 parameters (see table caption for definitions). For the correlations time averages over 1970-  
330 2000 or 2070-2100 are used. The correlations are not computed in the time- but in the model-  
331 domain (detailed equations are given in the supplementary material). We use all available  
332 models for these correlations. We did not remove outliers because there are no uniform metrics  
333 that define an outlier reliably. Sometimes one model seems to perform well for one variable but  
334 not for a different one. The strongest and significant correlation with the mean AMOC index at  
335 30°N in the model ensemble for both periods is found for the subpolar gyre (SPG) index ( $r_{\text{historical}}$   
336 = 0.87 and  $r_{\text{RCP4.5}} = 0.88$ ). The SPG index is defined here as the minimum of the barotropic  
337 streamfunction in the region 60°W-15°W / 45°N-65°N, and multiplied by -1. The SPG mean  
338 state is negative in the barotropic streamfunction, indicating anti-clockwise circulation, and our  
339 SPG index hence reflects the strength of this anti-clockwise circulation. Also the Atlantic mean  
340 meridional depth-integrated density difference (MDD) is significantly related to the AMOC

341 index ( $r_{\text{historical}} = 0.75$  and  $r_{\text{RCP4.5}} = 0.86$ ). A separation of MDD into salinity- and temperature-  
342 driven components ( $\text{MDD}_{\text{sal}}$  and  $\text{MDD}_{\text{temp}}$ ) suggests that salinity dominates this relationship,  
343 especially when the correlation of the differences is compared. Scatter plots between the AMOC  
344 index and density gradients from the CMIP3 and CMIP5 models (Fig. 4) show that a strong  
345 AMOC goes along with a large meridional density gradient. This relationship is in agreement  
346 with studies that incorporate simple box models of the Stommel type (Stommel 1961).  
347 However, we want to stress that the variability of the AMOC and general ocean circulation in  
348 a climate model is driven by more complex ocean-atmosphere interactions. The near-linear  
349 relationship between the AMOC index and the meridional density gradient (Fig. 4a) is primarily  
350 caused by the changes in salinity (Fig. 4c). Due to geostrophy, we also expect a dependence of  
351 the AMOC strength on the zonal density gradient (Sijp et al. 2012). However, the link between  
352 the AMOC index and the zonal density difference (ZDD) is weaker ( $r_{\text{historical}} = 0.63$  and  $r_{\text{RCP4.5}}$   
353  $= 0.62$ ; Fig. 4b) than the link to MDD, and changes in ZDD are only weakly related to projected  
354 changes in AMOC strength ( $r=0.16$ ). Further parameters that exhibit no strong correlation to  
355 the AMOC index are the northward Ekman transport at the southern border of the Atlantic  
356 ( $50^{\circ}\text{S}$ ) and the pycnocline depth.

357 As MDD appears to be closely related to the projected AMOC changes, a similar correlation  
358 analysis was performed to identify the factors most related to the MDD (Table 4). The  
359 freshwater flux at the ocean surface (WFO) seems to play a role in determining the mean  
360 meridional density gradient. We also considered integrating the freshwater flux over time for  
361 this analysis. However, this did not affect the relative importance of model uncertainty and  
362 internal variability, nor the signal-to-noise ratio. We find negative correlations with  $\text{WFO}_{\text{Arctic}}$   
363 (integrated over the Arctic;  $r_{\text{historical}} = -0.62$  and  $r_{\text{RCP4.5}} = -0.48$ ) and  $\text{WFO}_{30-50\text{N}}$  (integrated over  
364 the Atlantic  $30^{\circ}$ - $50^{\circ}\text{N}$ ;  $r_{\text{historical}} = -0.77$  and  $r_{\text{RCP4.5}} = -0.71$ ). But for the difference between the  
365 two periods there is no relationship ( $r_{\text{diff.}} = -0.03 / -0.10$ ). We point out that the validity of our

366 results in Tables 3 and 4 is limited. Low correlations with the AMOC index may be biased by  
367 strong model uncertainties. For example, the weak link of the ZDD with AMOC does not  
368 necessarily imply that the former is unrelated to AMOC strength or change. Instead, this may  
369 reflect differences in model dynamics. Furthermore, correlation analysis cannot identify causal  
370 links. However, in the following we will place emphasis on parameters with a high correlation  
371 to the AMOC strength or with the AMOC changes.

### 372 *Density structure*

373 All processes maintaining the density distribution in the water column are potentially important  
374 in steering the AMOC. Although virtually all models simulate a significant weakening of the  
375 AMOC under global warming conditions (Fig. 2), the reasons for changes and resulting  
376 feedback mechanisms in the individual models may differ, which is eventually reflected in a  
377 large model spread. In the 20<sup>th</sup> century runs, the simulated spatial and temporal distribution of  
378 the modeled temperature and salinity fields largely differ from model to model. Furthermore as  
379 mentioned above, the models suffer from large biases (e.g., Schneider et al. 2007).

380 The CMIP3 A1B (Fig 5a) and CMIP5 RCP4.5 (Fig. 5d) ensemble-mean projected changes in  
381 density, averaged zonally across the Atlantic, both show a strong reduction at the ocean surface,  
382 generally weakening with depth. The strongest surface density reduction occurs north of 40°N,  
383 with a secondary minimum near the Equator. The density signal penetrates relatively deep into  
384 the Arctic Ocean. In the Southern Hemisphere mid-latitudes near 45°S, the mean profiles show  
385 a strongly reduced density of the water column down to 1000 m depth. For some depth levels  
386 in CMIP5 RCP4.5, the Southern Hemisphere decrease in density is even larger than in the  
387 Arctic.

388 The impact on the density field through changes in temperature and salinity changes are also  
389 separated. The temperature effect dominates in the tropics and subtropics (Fig. 5b and 5e),



390 where it strongly reduces the density. Salinity on the other hand tends to enhance the density  
391 (Fig. 5c and 5f). A very strong salinity-induced increase in density is located around 30°N  
392 extending to a depth of about 1000 m. At higher latitudes, especially in the Arctic region, the  
393 models consistently project a strong salinity-induced reduction in density within the upper 1000  
394 m. The pattern in the salinity contribution to the density change might lead to an intensified  
395 meridional freshwater transport from the subtropics to the mid- and high latitudes, especially in  
396 the Northern Hemisphere. Enhanced sea ice melt and stronger river runoff into the subpolar  
397 North Atlantic and into the Arctic basin are also important in this context.

398 The largest uncertainties in the CMIP3 A1B projections of the density profiles (Fig. 6a and 6d)  
399 are located in the mid-latitude North Atlantic and Arctic with largest values close to the surface.  
400 Clearly, the overwhelming contribution to the total uncertainty in the projected density  
401 originates from the model uncertainty (Fig. 6b and 6e). By separating the model uncertainty in  
402 the density projections into a thermal- and a saline-driven part, it becomes also clear that the  
403 latter explains the major fraction of the model uncertainty, especially in the Arctic (Fig. 6c and  
404 6f). The results concerning the density changes from CMIP3 are basically confirmed by those  
405 from CMIP5, with the caveat that the changes in CMIP5 tend to be somewhat weaker. Some of  
406 this difference could be due to weaker radiative forcing of the RCP4.5 scenario used in CMIP5  
407 compared to the A1B scenario in CMIP3.

408 We now turn to the salinity projections themselves. The model uncertainty and the signal-to-  
409 noise ratios for both the CMIP3 and CMIP5 ensembles are estimated using the A1B and RCP4.5  
410 scenarios (Fig. 7). Consistent with the salinity contribution to the density uncertainty (Fig. 6c  
411 and 6f), the uncertainty in the salinity projections obtained from CMIP3 shows the largest  
412 uncertainties in the mid-latitude North Atlantic and in the Arctic (Fig. 7a and 7c). The  
413 uncertainty of the salinity projections obtained from the CMIP5 ensemble is much reduced  
414 compared to that calculated from the CMIP3 models. In the CMIP3 ensemble, a well distinct

415 region of high signal-to-noise ratio in the salinity projections is located in the region 20°N-  
416 40°N within the upper 700 m centered at a depth of about 300 m (Fig 7b). In the CMIP5  
417 ensemble, a similar pattern is found (Fig. 7d). However, the maximum values of the signal-to-  
418 noise ratio are somewhat smaller than in CMIP3. Still, the area where it exceeds unity is larger  
419 than in CMIP3. A gain in confidence is seen in a narrow region around 40°N below 700 m.  
420 Further regions of enhanced signal-to-noise ratio in CMIP5 are found in the Southern  
421 Hemisphere at 0°-20°S and south of 40°S, approximately in the upper 200 m. We conclude that  
422 the model uncertainty determines the uncertainty in the density projections by the end of the  
423 21<sup>st</sup> century, and that the uncertainty in the salinity projections is most relevant to the  
424 uncertainty in the density projections. In this study, we focus on the spread of model projections.  
425 Our results by no means imply that temperature changes are unimportant for the future  
426 evolution of the AMOC, but they appear to play a secondary role for the model uncertainty.

#### 427 *Freshwater budget*

428 We next investigate the projections for the freshwater flux integrated over the Arctic  
429 ( $WFO_{Arctic}$ ). In the CMIP5 ensemble, the projected changes in  $WFO_{Arctic}$  are anti-correlated with  
430 the changes in the AMOC index at 30°N (Table 3:  $r_{diff} = -0.68$ ). The projected mean  $WFO_{Arctic}$   
431 features some “outliers”, which does not allow drawing reliable conclusions. There also is a  
432 strong anti-correlation between mean  $WFO_{Arctic}$  and the meridional density gradient (Table 4:  
433  $r_{historical} = -0.62$  and  $r_{RCP4.5} = -0.48$ ). The projections of  $WFO_{Arctic}$  under the A1B (CMIP3) and  
434 RCP4.5 (CMIP5) scenarios both show a negative ensemble-mean trend (Fig. 8a and 8d), which  
435 leads to a freshening of the Arctic. However, the spread among individual models is large. In  
436 the CMIP5 projections (Fig. 8e), the model uncertainty is remarkably reduced compared to  
437 CMIP3 (Fig. 8b). This improvement could be caused by the higher complexity of the CMIP5  
438 models that among others employ higher resolution. As a consequence, small-scale processes  
439 influencing evaporation, precipitation, river runoff, and/or sea ice can be more realistically

440 simulated. Consistent with this, the signal-to-noise ratio (Fig. 8c and 8f) is larger in CMIP5, but  
441 it does not exceed 1.2. Uncertainty in freshwater flux affects the surface salinity in the Arctic  
442 and also remote regions by advection. The large uncertainty in surface salinity north of 40°N  
443 (Fig. 7) is at least partially explained by the highly uncertain freshwater budget. However, the  
444 projected changes in  $WFO_{Arctic}$  and in MDD (for 2070-2100 relative to 1970-2000) are not  
445 significantly correlated in the CMIP5 ensemble (Table 4:  $r_{diff.} = -0.03$ ), underscoring the  
446 complexity of freshwater processes in the climate models.

#### 447 *Subpolar Gyre index*

448 Our results suggest that the processes in the northern North Atlantic are most important for the  
449 model uncertainties in the AMOC. This is equally confirmed by both CMIP3 and CMIP5.  
450 Therefore, our following analysis on the subpolar gyre (SPG) index is only based on the CMIP5  
451 model ensemble. The models project an ensemble-mean reduction in the SPG index until 2100  
452 in both scenarios (RCP4.5 and RCP8.5). The SPG index during the reference period (1970-  
453 2000) is 42.3 Sv, with a projected weakening until 2090-2100 of 10.6 Sv in RCP4.5 and 13.8  
454 Sv in RCP8.5, i.e. a reduction of about 25% and 33%, respectively. The SPG and the AMOC  
455 indices are highly correlated across the model ensemble (Table 3:  $r_{historical} = 0.87$  and  $r_{RCP4.5} =$   
456  $0.88$ ). However, the correlation between the projected changes of these two periods is weak  
457 ( $r_{diff.} = 0.17$ ). The large model spread of the SPG projection (Fig. 9a) results in high model  
458 uncertainty, which is much higher than the internal variability and scenario uncertainty (Fig.  
459 9b). This is reflected in a signal-to-noise ratio less than unity during the entire 21<sup>st</sup> century (Fig.  
460 9c). Therefore, a weakening of the SPG in the ensemble-mean is not significant, due to the large  
461 model uncertainty, which is possibly also affecting the AMOC strength.

462 The SPG index is obtained from the barotropic streamfunction, which can be split into a wind-  
463 driven flat-bottom Sverdrup transport and into a bottom pressure torque-driven transport  
464 (Greatbatch et al. 1991). We compute the uncertainties of the flat-bottom Sverdrup transport to

465 evaluate the importance of wind stress projections in generating this high model uncertainty in  
466 the SPG. We find that model uncertainty for the total barotropic streamfunction (Fig. 10a) is  
467 much larger than for the flat-bottom Sverdrup transport (Fig. 10b). Therefore, we eliminate  
468 wind stress as a potential source for high model uncertainty in the SPG. The remaining potential  
469 source is the bottom pressure torque, which depends on bottom pressure (vertically integrated  
470 density) and on bottom topography. We conclude that model differences in density projections  
471 and potentially also the different spatial representations of the bathymetry are responsible for  
472 the high uncertainty in the SPG index projections. In fact, we find that models with a higher  
473 vertical resolution tend to simulate a stronger SPG and also a stronger weakening over the 21<sup>st</sup>  
474 century (for details see the supplementary material).

#### 475 **4. Summary and discussion**

476 We have investigated the Atlantic Meridional Overturning Circulation (AMOC) projections for  
477 the 21<sup>st</sup> century obtained from the CMIP3 and CMIP5 ensembles. The CMIP5 model  
478 projections indicate a weakening of the AMOC of approximately 25% by the end of the 21<sup>st</sup>  
479 century, in agreement with the CMIP3 projections. However, the spread in CMIP5 AMOC  
480 projections is substantially larger than that in CMIP3. The model uncertainty is by far the largest  
481 contribution to the total AMOC projection uncertainty in both model ensembles. Nevertheless,  
482 by investigating the AMOC index at 30°N to compute the signal-to-noise ratio in the subtropics,  
483 which is based on the 90%-confidence level, we find that it is sufficiently large to detect an  
484 anthropogenic AMOC signal by 2030 in both CMIP3 and CMIP5. The signal-to-noise ratio is  
485 less favorable in the mid-latitude North Atlantic, which was inferred by investigating the  
486 AMOC index at 48°N.

487 At lead times of several decades and longer, the model uncertainty becomes much larger than  
488 the scenario uncertainty - even toward the end of the 21<sup>st</sup> century. In contrast to this, the globally  
489 averaged surface air temperature uncertainties are at these long lead times dominated by

490 scenario uncertainty (Hawkins and Sutton 2009). Finally, we conclude that the AMOC  
491 projection uncertainty due to internal variability is unimportant at lead times beyond a few  
492 decades. Likewise, the uncertainty originating from mechanical forcing of the AMOC by  
493 atmospheric wind stress is insignificant in comparison to other sources of uncertainties. Thus,  
494 the AMOC model uncertainty appears to be dominated by the model uncertainty in projecting  
495 the oceanic density structure. The uncertainty in the projection of the density increases with  
496 latitude and is particularly strong in the subpolar North Atlantic and in the Arctic. The model  
497 uncertainties in the salinity projections explain most of the uncertainty that is found in the  
498 density projections. Salinity uncertainty in turn might be caused by uncertainties arising from  
499 freshwater flux and gyre-strength projections. The latter is important, because the strength of  
500 the SPG influences the salt advection into the regions of deep water formation. As in the salinity  
501 projections, the freshwater flux and gyre-strength projections depict large uncertainties in high  
502 latitudes. This could possibly be a reason for the large uncertainty in projecting the 21<sup>st</sup> century  
503 AMOC. Given our incomplete understanding of the AMOC, making a quantitative assessment  
504 of AMOC changes remains a challenge. Nevertheless, we can conclude that model  
505 improvements that affect the density structure in the North Atlantic will lead to a more reliable  
506 AMOC projection.

507 **Acknowledgements:**

508 We acknowledge the World Climate Research Programme's Working Group on Coupled  
509 Modelling, which is responsible for CMIP, and we thank the climate modeling groups for  
510 producing and making available their model output. For CMIP the U.S. Department of Energy's  
511 Program for Climate Model Diagnosis and Intercomparison (PCDMI) provides coordinating  
512 support and led development of software infrastructure in partnership with the Global  
513 Organization for Earth System Science Portals. This work was supported by the North Atlantic  
514 and the RACE Project of BMBF (grant agreement no. 03F0651B) and the European Union FP7

515 NACLIM project (grant agreement no. 308299). N.K. acknowledges support from the Deutsche  
516 Forschungsgemeinschaft under the Emmy Noether-Programm (grant KE 1471/2-1) and the  
517 NFR EPOCASA project (grant 229774/E10).

518 **Conflict of Interest:**

519 The authors declare that they have no conflict of interest.

520 **References:**

- 521 Ba J, Keenlyside NS, Latif M, Park W, Ding H, Lohmann K, Mignot J, Menary M, Otterå  
522 OH, Wouters B, Salas y Melia D, Oka A, Bellucci A, Volodin E (2014) A multi-model  
523 comparison of Atlantic multidecadal variability. *Clim Dyn* 43:2333–2348
- 524 Collins M, Knutti R, Arblaster J, Dufresne J-L, Fichet T, Friedlingstein P, Gao X, Gutowski  
525 WJ, Johns T, Krinner G, Shongwe M, Tebaldi C, Weaver AJ, Wehner M (2013) Long-term  
526 Climate Change: Projections, Commitments and Irreversibility. In: Stocker TF, Qin D,  
527 Plattner G-K, Tignor M, Allen SK, Boschung J, Nauels A, Xia Y, Bex V, Midgley PM (eds)  
528 Climate Change 2013: The Physical Science Basis. Contribution of Working Group I to the  
529 Fifth Assessment Report of the Intergovernmental Panel on Climate Change, Cambridge  
530 University Press, Cambridge, United Kingdom and New York, NY, USA
- 531 Cunningham SA, Kanzow T, Rayner D, Baringer MO, Johns WE, Marotzke J, Longworth  
532 HR, Grant EM, Hirschi JJ-M, Beal LM, Meinen CS, Bryden HL (2007) Temporal Variability  
533 of the Atlantic Meridional Overturning Circulation at 26.5°N. *Science* 317:935-938
- 534 Danabasoglu G (2008) On Multidecadal Variability of the Atlantic Meridional Overturning  
535 Circulation in the Community Climate System Model Version 3. *J Clim* 21:5524-5544
- 536 de Boer AM, Gnanadesikan A, Edwards NR, Watson AJ (2010) Meridional Density Gradients  
537 Do Not Control the Atlantic Overturning Circulation. *J Phys Oceanogr* 40:368–380
- 538 Delworth T, Manabe S, Stouffer RJ (1993) Interdecadal Variations of the Thermohaline  
539 Circulation in a Coupled Ocean-Atmosphere Model. *J Clim* 6:1993-2011
- 540 Delworth TL, Zeng F (2012) Multicentennial variability of the Atlantic meridional  
541 overturning circulation and its climatic influence in a 4000 year simulation of the GFDL  
542 CM2.1 climate model. *Geophys Res Lett* 39:L13702

543 Dickson RR, Brown J (1994) The production of North Atlantic Deep Water: Sources, rates,  
544 and pathways. *J Geophys Res* 99:12319–12341

545 Ganachaud A, Wunsch C (2003) Large-Scale Ocean Heat and Freshwater Transports during  
546 the World Ocean Circulation Experiment. *J Clim* 16:696-705

547 Gnanadesikan A (1999) A Simple Predictive Model for the Structure of the Oceanic  
548 Pycnocline. *Science* 283:2077-2079

549 Gulev SK, Latif M, Keenlyside N, Park W, Koltermann KP (2013) North Atlantic Ocean  
550 control on surface heat flux on multidecadal timescales. *Nature* 499:464-467

551 Greatbatch RJ, Fanning AF, Goulding AD, Levitus S (1991) A Diagnosis of Interpentadal  
552 Circulation Changes in the North Atlantic. *J Geophys Res* 96:22009-22023

553 Hawkins E, Sutton R (2009) The potential to narrow uncertainty in regional climate  
554 predictions. *Bull Am Meteorol Soc* 90:1095-1107

555 Hawkins E, Sutton R (2011): The potential to narrow uncertainty in projections of regional  
556 precipitation change. *Clim Dyn* 37:407-418

557 Knight JR, Allan RJ, Folland CK, Vellinga M, Mann ME (2005) A signature of persistent  
558 natural thermohaline circulation cycles in observed climate. *Geophys Res Lett* 32:L20708

559 Kuhlbrodt T, Griesel A, Montoya M, Levermann A, Hofmann M, Rahmstorf S (2007) On the  
560 driving processes of the Atlantic meridional overturning circulation. *Rev Geophys* 45:1–32

561 Latif M, Keenlyside NS (2011) A Perspective on Decadal Climate Variability and  
562 Predictability. *Deep Sea Res II* 58:1880-1894

563 Latif M, Roeckner E, Botzet M, Esch M, Haak H, Hagemann S, Jungclaus J, Legutke S,  
564 Marsland S, Mikolajewicz U, Mitchell J (2004) Reconstructing, Monitoring, and Predicting



565 Multidecadal-Scale Changes in the North Atlantic Thermohaline Circulation with Sea Surface  
566 Temperature. *J Clim* 17:1605-1614

567 Masson D, Knutti R (2011) Climate model genealogy. *Geophys Res Lett* 38:L08703

568 McCarthy G, Frajka-Williams E, Johns WE, Baringer MO, Meinen CS, Bryden HL, Rayner  
569 D, Duchez A, Roberts C, Cunningham SA (2012) Observed interannual variability of the  
570 Atlantic meridional overturning circulation at 26.5°N. *Geophys Res Lett* 39:L19609  
571 Mecking JV, Keenlyside NS, Greatbatch RJ (2014) Stochastically-forced multidecadal variability in the  
572 North Atlantic: a model study. *Clim Dyn* 43: 271-288

573 Meehl GA, Covey C, Delworth T, Latif M, McAvaney B, Mitchell JFB, Stouffer RJ, Taylor  
574 KE (2007a) The WCRP CMIP3 multi-model dataset: A new era in climate change research.  
575 *Bull Am Meteorol Soc* 88:1383-1394

576 Meehl GA, Stocker TF, Collins WD, Friedlingstein P, Gaye AT, Gregory JM, Kitoh A, Knutti  
577 R, Murphy JM, Noda A, Raper SCB, Watterson IG, Weaver AJ, Zhao Z-C (2007b) Global  
578 Climate Projections. In: Solomon S, Qin D, Manning M, Chen Z, Marquis M, Averyt KB,  
579 Tignor M, Miller HL (eds) *Climate Change 2007: The Physical Science Basis. Contribution*  
580 *of Working Group I to the Fourth Assessment Report of the Intergovernmental Panel on*  
581 *Climate Change*, Cambridge University Press, Cambridge, United Kingdom and New York,  
582 NY, USA

583 Park W, Latif M (2008) Multidecadal and Multicentennial Variability of the Meridional  
584 Overturning Circulation. *Geophys Res Lett* 35:L22703

585 Park W, Latif M (2012) Atlantic Meridional Overturning Circulation response to idealized  
586 external forcing. *Clim Dyn* 39:1709-1726

587 Park T, Park W, Latif M (2016) Correcting North Atlantic Sea Surface Salinity Biases in the  
588 Kiel Climate Model: Influences on Ocean Circulation and Atlantic Multidecadal Variability.  
589 *Clim Dyn*, in press

590 Roberts CD, Jackson L, McNeall D (2014) Is the 2004–2012 reduction of the Atlantic  
591 meridional overturning circulation significant? *Geophys Res Lett* 41:3204–3210

592 Robson J, Hodson D, Hawkins E, Sutton R (2014) Atlantic overturning in decline? *Nature*  
593 7:2-3

594 Schmittner A, Latif M, Schneider B (2005) Model projections of the North Atlantic  
595 thermohaline circulation for the 21st century assessed by observations. *Geophys Res Lett*  
596 32:L23710

597 Schneider B, Latif M, Schmittner A (2007). Evaluation of different methods to assess model  
598 projections of the future evolution of the Atlantic Meridional Overturning Circulation. *J Clim*  
599 20:2121-2132

600 Shakespeare CJ, Hogg AM (2012) An Analytical Model of the Response of the Meridional  
601 Overturning Circulation to Changes in Wind and Buoyancy Forcing. *J Phys Oceanogr*  
602 42:1270-1287

603 Sijp, WP, Bates M, England MH (2006) Can isopycnal mixing control the stability of the  
604 thermohaline circulation in ocean climate models? *J Clim* 19:5637-5651

605 Sijp, WP, Gregory JM, Tailleux R, Spence P (2012) The Key Role of the Western Boundary  
606 in Linking the AMOC Strength to the North-South Pressure Gradient. *J Phys Oceanogr*  
607 42:628-643

608 Smeed DA, McCarthy GD, Cunningham SA, Frajka-Williams E, Rayner D, Johns WE,  
609 Meinen CS, Baringer MO, Moat BI, Duchez A, Bryden HL (2014) Observed decline of the  
610 Atlantic meridional overturning circulation 2004-2012. *Ocean Sci* 10:29–38

611 Srokosz M, Baringer M, Bryden H, Cunningham S, Delworth T, Lozier S, Marotzke J, Sutton  
612 R (2012) Past, present and future change in the Atlantic meridional overturning circulation.  
613 *Bull Am Meteorol Soc* 93:1663-1676

614 Stommel H (1961) Thermohaline convection with two stable regimes of flow. *Tellus*  
615 13(2):224-230

616 Sutton RT, Hodson DLR (2005) North Atlantic Forcing of North American and European  
617 Summer Climate. *Science* 309:115-118

618 Taylor KE, Stouffer RJ, Meehl GA (2012) An Overview of CMIP5 and the experiment  
619 design. *Bull Am Meteorol Soc* 93:485-498

620 Thorpe RB, Gregory JM, Johns TC, Wood RA, Mitchell JFB (2001) Mechanisms determining  
621 the Atlantic thermohaline circulation response to greenhouse gas forcing in a non-flux-  
622 adjusted coupled climate model. *J Clim* 14:3102–3116

623 Visbeck M, Chassignet EP, Curry R, Delworth T, Dickson B, Krahnemann G (2003) The  
624 ocean's response to North Atlantic Oscillation variability. In: Hurrell JW, Kushnir Y, Ottensen  
625 G, Visbeck M (eds) *The North Atlantic Oscillation: Climatic Significance and Environmental*  
626 *Impact*, Geophysical Monograph Series, American Geophysical Union, Washington DC, pp  
627 113-145

628 Wang C, Zhang L, Lee S, Wu L, Mechoso CR (2014) A global perspective on CMIP5 climate  
629 model biases. *Nat Clim Change* 4:201-205

630 Yip S, Ferro CAT, Stephenson DB, Hawkins E (2011) A simple, coherent framework for  
631 partitioning uncertainty in climate predictions. J Clim 24:4634-4643

632 Zhang R, Delworth TL (2006) Impact of Atlantic multidecadal oscillations on India/Sahel  
633 rainfall and Atlantic hurricanes. Geophys Res Lett 33:L17712

634

635

636 **Tables**

637 Table 1

CMIP3	AMOC			Salinity	Pot. T.	WFO	M <sub>y</sub>
	A1B	A2	B1				
BCCR-BCM2.0	X	X	X	X	X		
CGCM3.1(T47)	X	X	X	X	X	X	X
CGCM3.1(T63)	X			X	X	X	X
CNRM-CM3	X			X	X	X	X
CSIRO-Mk3.0	X	X		X	X	X	X
CSIRO-Mk3.5	X	X	X	X	X	X	X
GFDL-CM2.0	X			X	X	X	X
GFDL-CM2.1	X	X	X	X		X	X
GISS-AOM	X		X	X	X		X
GISS-ER	X	X	X	X	X	X	X
INM-CM3.0	X	X	X			X	X
IPSL-CM4	X	X	X	X	X		X
MIROC3.2(hires)	X		X	X	X		X
MIROC3.2(medres)	X	X	X	X	X	X	X
MIUB-ECHO-G	X	X	X	X	X	X	X
MPI-ECHAM5	X	X	X	X	X	X	X
MRI-CGCM2.3.2a	X	X	X	X	X	X	X
NCAR-CCSM3	X						X
NCAR-PCM1	X			X	X		X
UKMO-HadCM3	X			X	X	X	X

638

639 **Table 1** Models of CMIP3. The compiled dataset for the variables AMOC (Atlantic Meridional  
640 Overturning Circulation), salinity, potential temperature, WFO (freshwater flux), and M<sub>y</sub>  
641 (northward Ekman transport). Scenarios for the 21<sup>st</sup> century are marked in addition to the  
642 20C3M scenario.

643

644 Table 2

CMIP5	AMOC	Salinity	Pot. Temp.	WFO	$\Psi$	$\tau$
	RCP45 & RCP85	RCP45			RCP45 & RCP85	
ACCESS1.3	X	X	X	X		
BCC-CSM1.1		X	X			
CanESM2	X	X	X		X	X
CCSM4	X	X	X		X	X
CESM1-BGC	X	X	X		X	X
CESM1-CAM5	X	X	X		X	X
CESM1-CAM5.1,FV2	X					
CESM1-WACCM	X	X	X		X	X
CMCC-CM		X	X	X		
CMCC-CMS		X	X	X		
CNRM-CM5	X	X	X	X	X	X
CSIRO-Mk3.6.0		X	X	X		
FGOALS-g2	X	X	X			
GFDL-CM3	X	X	X	X	X	X
GFDL-ESM2G 210		X	X	X	X	X
GFDL-ESM2M	X	X	X	X	X	X
GISS-E2-H		X	X			
GISS-E2-R		X	X			
Had-GEM2-AO		X	X			
Had-GEM2-CC		X	X	X		
Had-GEM2-ES		X	X	X		
IPSL-CM5A-LR		X	X	X		
IPSL-CM5A-MR		X	X	X		
IPSL-CM5B-LR		X	X	X		
MIROC-ESM		X	X	X		
MIROC-ESM-CHEM				X		
MIROC5	X	X	X	X		
MPI-ESM-LR	X	X	X	X	X	X
MPI-ESM-MR	X	X	X	X	X	X
MRI-CGCM3	X	X	X	X	X	X
NorESM1-M	X	X	X	X	X	X
NorESM1-ME	X	X	X	X	X	X

645  
646 **Table 2** Models of CMIP5. The compiled dataset for the variables AMOC (Atlantic Meridional  
647 Overturning Circulation), salinity, potential temperature, WFO (freshwater flux),  $\Psi$  (barotropic  
648 streamfunction including the subpolar gyre index), and  $\tau$  (wind stress – used for computing the  
649 flat-bottomed Sverdrup transport and the northward Ekman transport). Scenarios for the 21<sup>st</sup>  
650 century are marked in addition to the historical scenario.

651 Table 3

	AMOC		
	1970-2000 (historical)	2070-2100 (RCP4.5)	diff.
$H^2$	<b>0.52</b>	<b>0.54</b>	<b>0.51</b>
MDD 74°N – 30°S	<b>0.75</b>	<b>0.86</b>	<b>0.55</b>
MDD <sub>sal</sub>		<b>0.83</b>	<b>0.60</b>
MDD <sub>temp</sub>		<b>0.65</b>	<b>-0.56</b>
$H^2$ MDD	<b>0.72</b>	<b>0.82</b>	<b>0.64</b>
WFO <sub>Arctic</sub>	-0.53	-0.13	<b>-0.68</b>
WFO <sub>subpolar</sub>	0.43	<b>-0.66</b>	0.25
WFO <sub>Nordic Seas</sub>	<b>0.78</b>	0.51	<b>0.58</b>
WFO <sub>30-50N</sub>	<b>-0.81</b>	<b>-0.65</b>	0.45
WFO <sub>trop. NA</sub>	<b>-0.85</b>	<b>-0.8</b>	0.32
Ekman transport (50°S, 70°W-25°E)	-0.03	-0.16	-0.12
Pycnocline depth (20°N-20°S)	<b>0.45</b>	0.26	-0.1
ZDD (30°N, 70°W-20°W)	<b>0.63</b>	<b>0.62</b>	0.16
Subpolar Gyre index	<b>0.87</b>	<b>0.88</b>	0.17
Subtropical Gyre index	0.08	-0.03	<b>0.61</b>

652

653 **Table 3** Correlations between different parameters and the Atlantic Meridional Overturning

654 Circulation (AMOC) index at 30°N in the CMIP5 model ensemble. Correlation coefficients are given

655 in three columns. The first is related to the mean of during periods 1970-2000 (historical), the second

656 during 2070-2100 (RCP4.5) and the third to the differences between these two periods (diff.). The

657 parameters used in the table are: the squared depth of the stream function ( $H^2$ ); the meridional density

658 difference (MDD) between 74°N and 30°S down to 1400m depth and averaged across the Atlantic; the

659 temperature contribution to the MDD change computed using the salinity profile of the years 1970-

660 2000 (MDD<sub>temp</sub>) and the salinity contribution using the temperature profile of the years 1970-2000661 (MDD<sub>sal</sub>); the freshwater flux into the Arctic basin including the Barents Sea and Kara Sea region662 (WFO<sub>Arctic</sub>); the freshwater flux into Atlantic ocean between 50°N and 65°N excluding the Norwegian663 Sea (WFO<sub>subpolar</sub>); the freshwater flux into the Norwegian Sea, Greenland Sea and Iceland Sea664 (WFO<sub>Nordic Seas</sub>); the freshwater flux into the Atlantic between 30°N and 50°N (WFO<sub>30-50N</sub>); the665 freshwater flux into the Atlantic between 0° and 30°N (WFO<sub>trop. NA</sub>); the Ekman transport at 50°S in

666 the Atlantic sector (70°W-25°E); the pycnocline depth according to Gnanadeskian (1999); the zonal

667 density difference (ZDD); the Subpolar Gyre index (the minimum in the barotropic streamfunction

668 within the area 60°-15°W / 45°-65°N multiplied by -1); the Subtropical Gyre index (the maximum



669 in the barotropic streamfunction within the area  $80^{\circ}$ - $40^{\circ}$ W /  $15^{\circ}$ - $45^{\circ}$ N). Bold numbers are significant  
670 at the 90%-confidence level. The critical correlation coefficient varies because a different number of  
671 models was used depending on the variables.

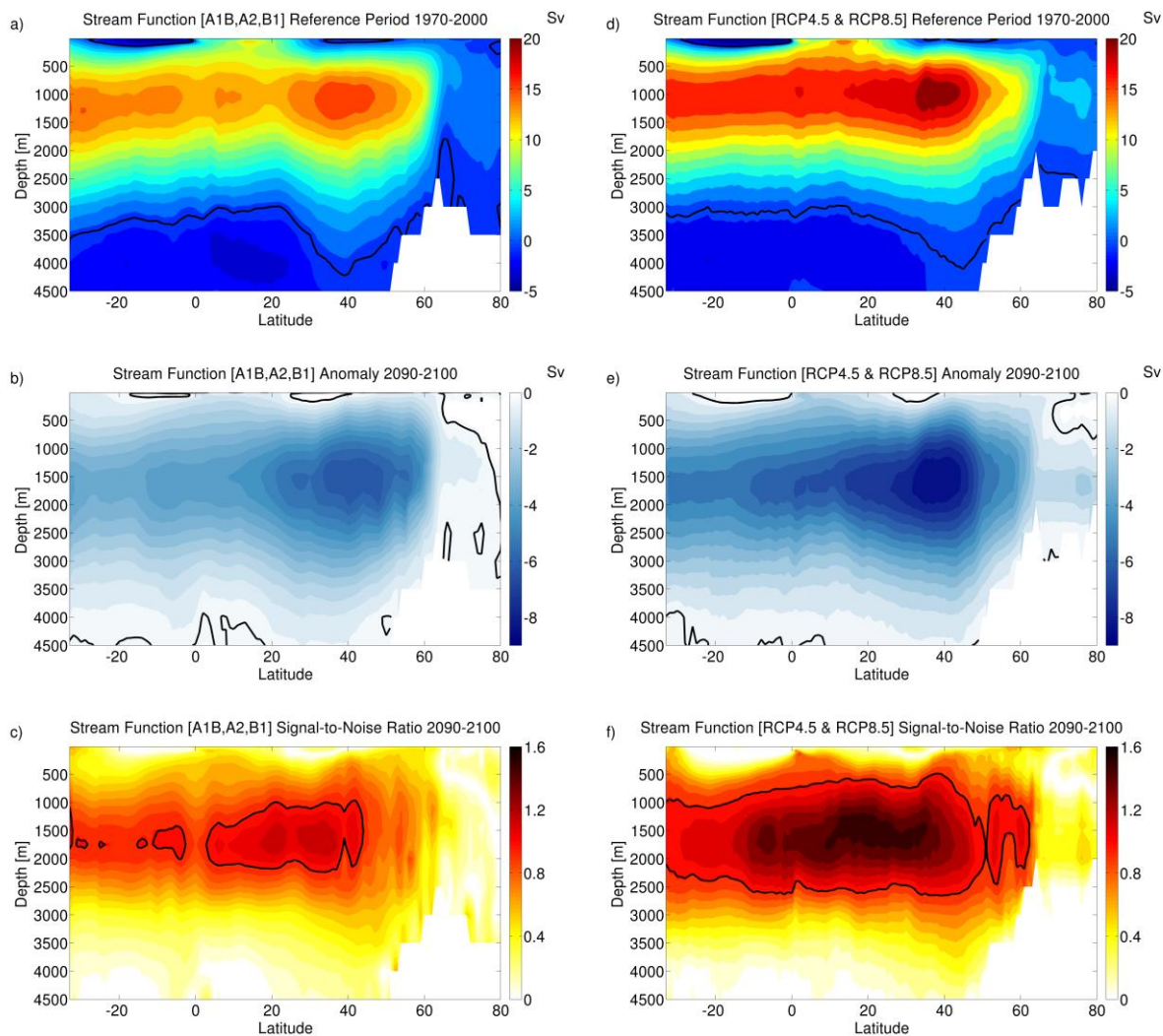
672 Table 4

	MDD		
	1970-2000 (historical)	2070-2100 (RCP4.5)	diff.
H <sup>2</sup>	<b>0.43</b>	<b>0.54</b>	0.04
WFO <sub>Arctic</sub>	<b>-0.62</b>	<b>-0.48</b>	-0.03
WFO <sub>subpolar</sub>	0.08	-0.40	-0.38
WFO <sub>Nordic Seas</sub>	<b>0.44</b>	0.39	0.06
WFO <sub>30-50N</sub>	<b>-0.77</b>	<b>-0.71</b>	-0.10
WFO <sub>trop. NA</sub>	0.02	-0.01	0.32

673

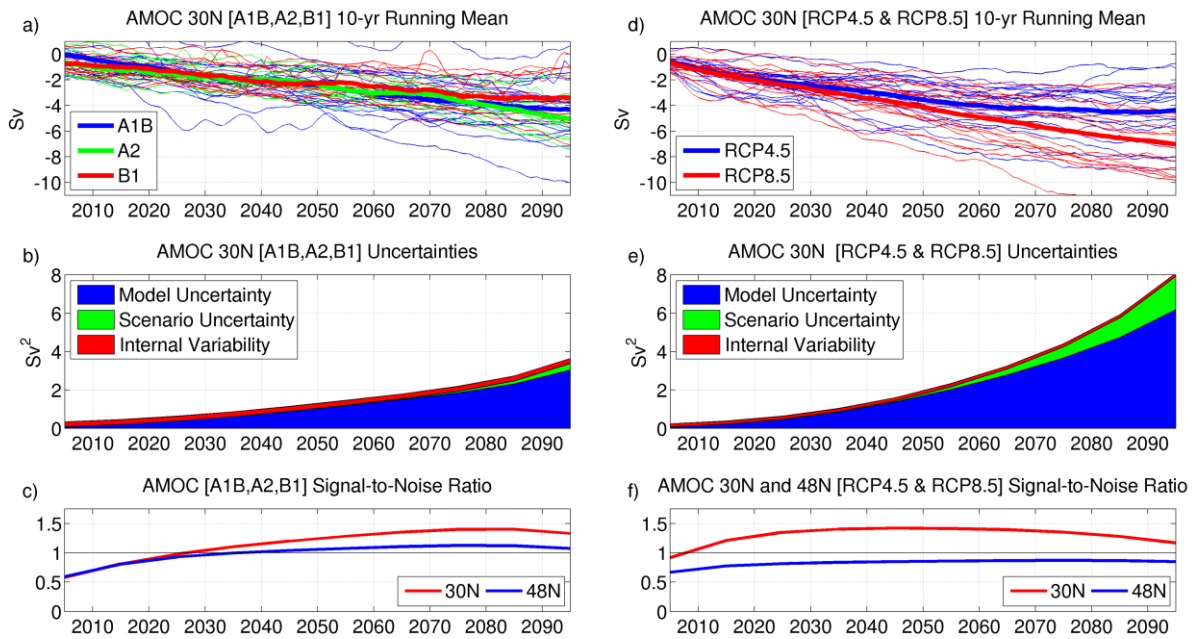
674 **Table 4** Correlations analogous to Table 3 but for the meridional density difference (MDD) between  
675 74°N and 30°S down to 1400m depth instead of the Atlantic Meridional Overturning Circulation  
676 (AMOC) index. Bold numbers are significant at the 90%-confidence level. The critical correlation  
677 coefficient varies because a different number of models was used depending on the variables.

678



680

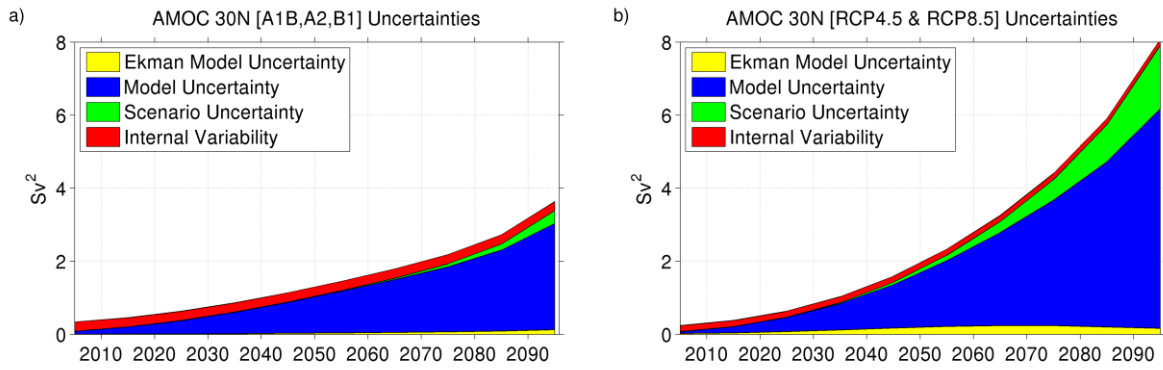
681 **Fig. 1** The Atlantic meridional overturning streamfunction for CMIP3 and CMIP5 from the  
 682 models listed in Table 1 and Table 2. Panels (a-c) summarizes the results for CMIP3 (20C3M,  
 683 SRES A1B, A2 and B1 scenarios), and the panels (d-f) provide the results for CMIP5  
 684 (historical, RCP4.5 and RCP8.5 scenarios). (a, d) ensemble-mean overturning streamfunction  
 685 ( $Sv = 10^6 \text{ m}^3/\text{s}$ ) for the reference period year 1970-2000. (b, e) anomaly by 2090-2100 relative  
 686 to the reference period 1970-2000. (c, f) signal-to-noise ratio with the 90%-confidence limit  
 687 given by the black contour. Please note the different scales in the color bars



688

689 **Fig. 2** Sources of the uncertainties in projections of the AMOC until 2100. a-c: CMIP3 (SRES  
 690 A1B, A2 and B1). (d-f) CMIP5 (RCP4.5 and RCP8.5). (a) and (d): AMOC long-term changes  
 691 of the individual models at 30°N; the 10-year running mean is presented (the climate mean of  
 692 the reference period 1970-2000 has been removed). (b) and (e): individual absolute  
 693 uncertainties of the AMOC projections ( $Sv^2$ ) at 30°N. (c) and (f): signal-to-noise ratio for the  
 694 AMOC changes at 30°N (red) and 48°N (blue)

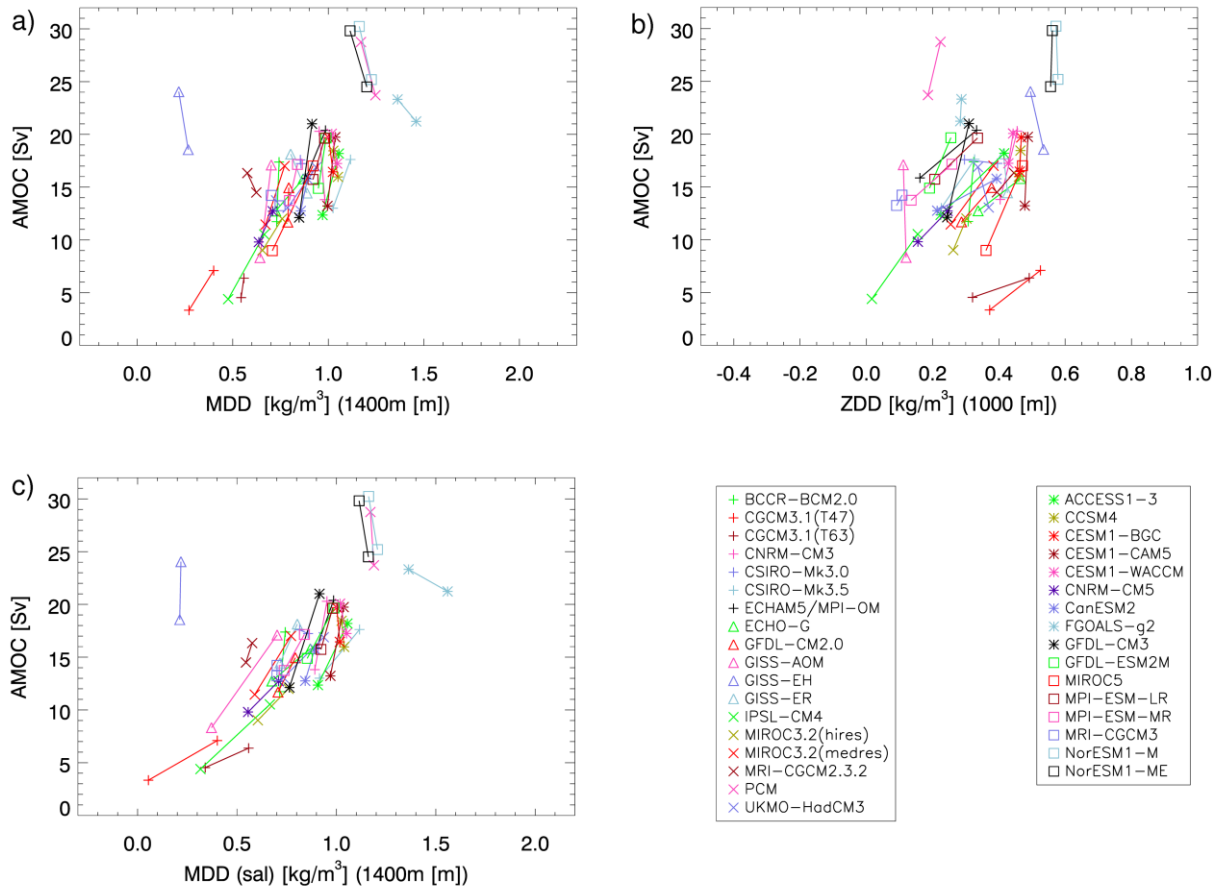
695



696

697 **Fig. 3** Absolute uncertainties of the AMOC (Atlantic Meridional Overturning Circulation)  
 698 projections at 30°N in CMIP3 ( $Sv = 10^6 \text{ m}^3/\text{s}$ ). The figures are the same as Figs. 2b and 2e  
 699 except that they include the contribution of the wind-driven meridional Ekman transport to the  
 700 model uncertainty (yellow). **(a)** for CMIP3 with the scenarios A1B, A2, and B1. **(b)** for CMIP5  
 701 with the scenarios RCP4.5 and RCP8.5

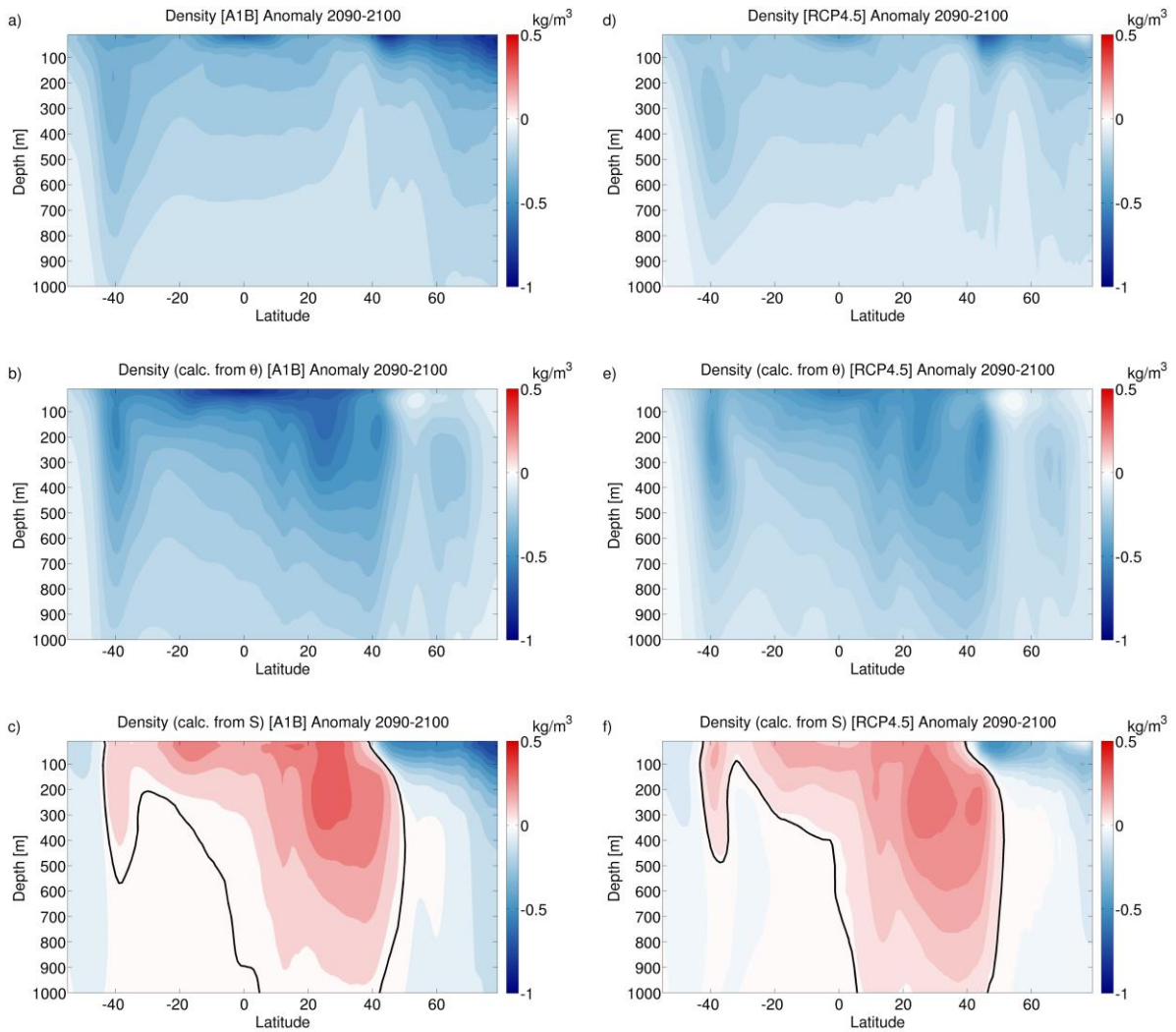
702



703

704 **Fig. 4** AMOC index at 30°N and (a) meridional density difference (MDD) between 74°N and  
 705 30°S, (b) zonal density difference (ZDD) at 30°N. (c): same as (a) but the 21<sup>st</sup> century density  
 706 includes only the salinity effect, i.e. temperature profile of CMIP3 (CMIP5) has been taken  
 707 from 20C3M (historical). Each symbol represents one model; the line connects the symbols for  
 708 the 20C3M (historical) run averaged over 1970-2000 with the SRES A1B (RCP4.5) run  
 709 averaged over 2070-2100

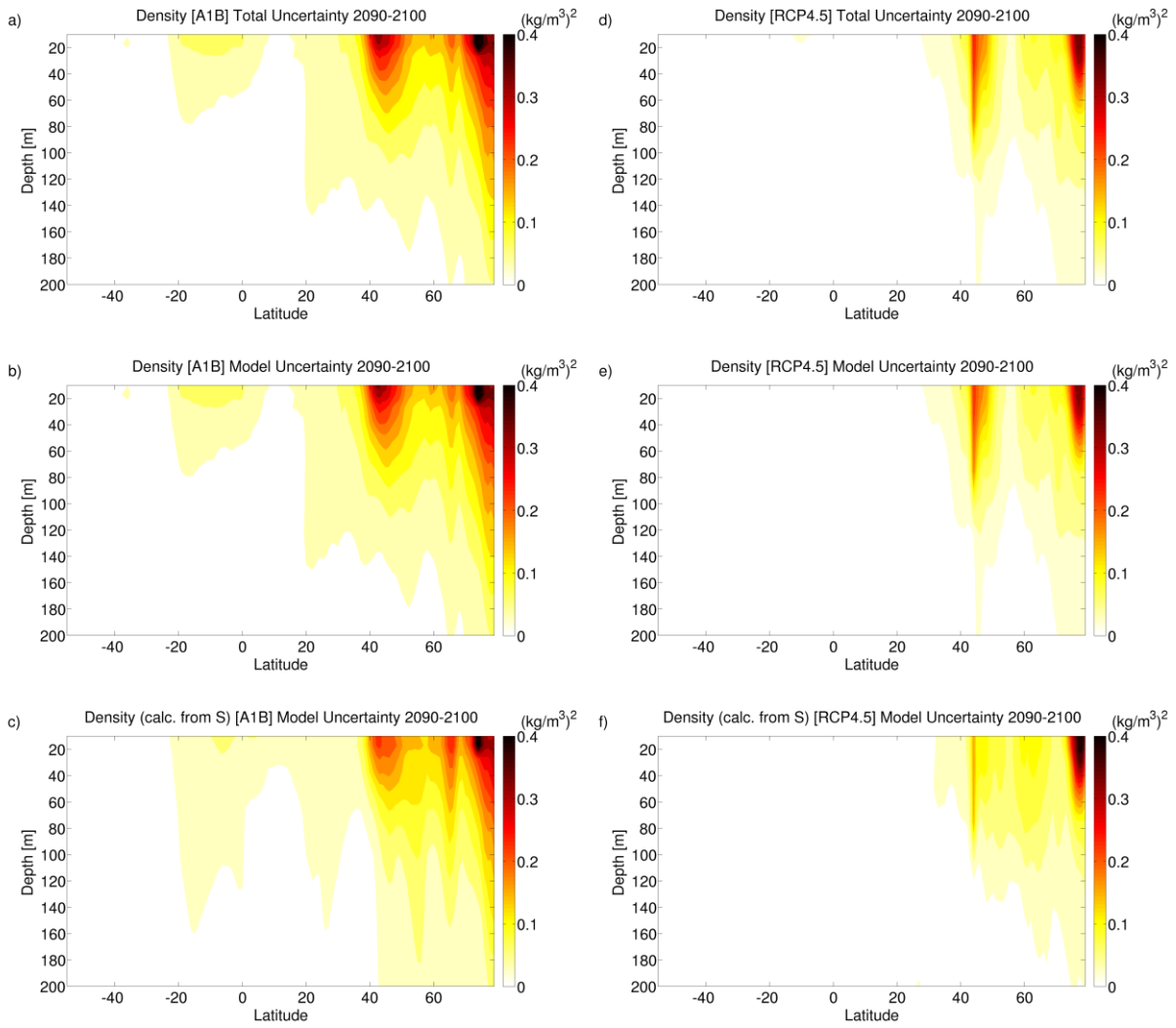
710



711

712 **Fig. 5** Density anomaly projections for CMIP3 (**a-c**) and CMIP5 (**d-f**). a and d: The Atlantic  
 713 basin meridional profiles of the ensemble mean potential density anomalies 2090-2100 relative  
 714 to 1970-2000. (**b**) and (**e**): density anomaly based only on the projected changes in potential  
 715 temperature. (**c**) and (**f**): density anomaly based only on the projected changes in salinity

716

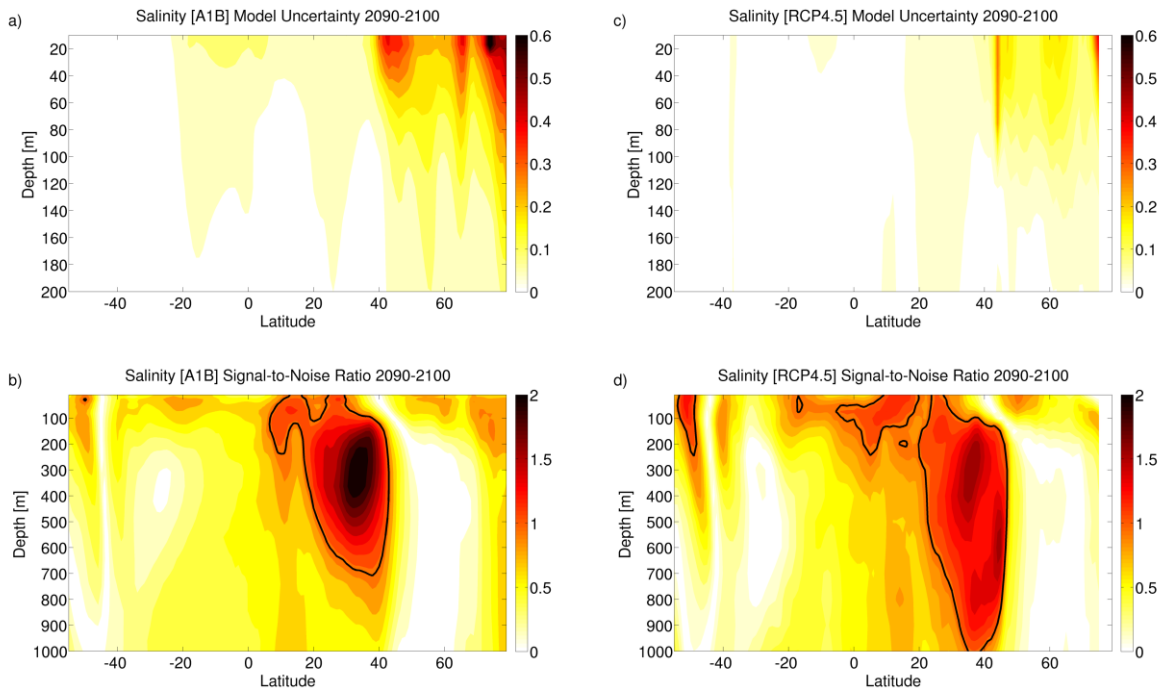


717

718 **Fig. 6** Uncertainties in the density projections for CMIP3 (a-c) and CMIP5 (d-f). (a) and (d):  
 719 the total uncertainties in the density projection. (b) and (e): the model uncertainty in the density  
 720 projection. (c) and (f): the model uncertainty in the density projection based only on salinity  
 721 projections (temperature is kept constant)

722

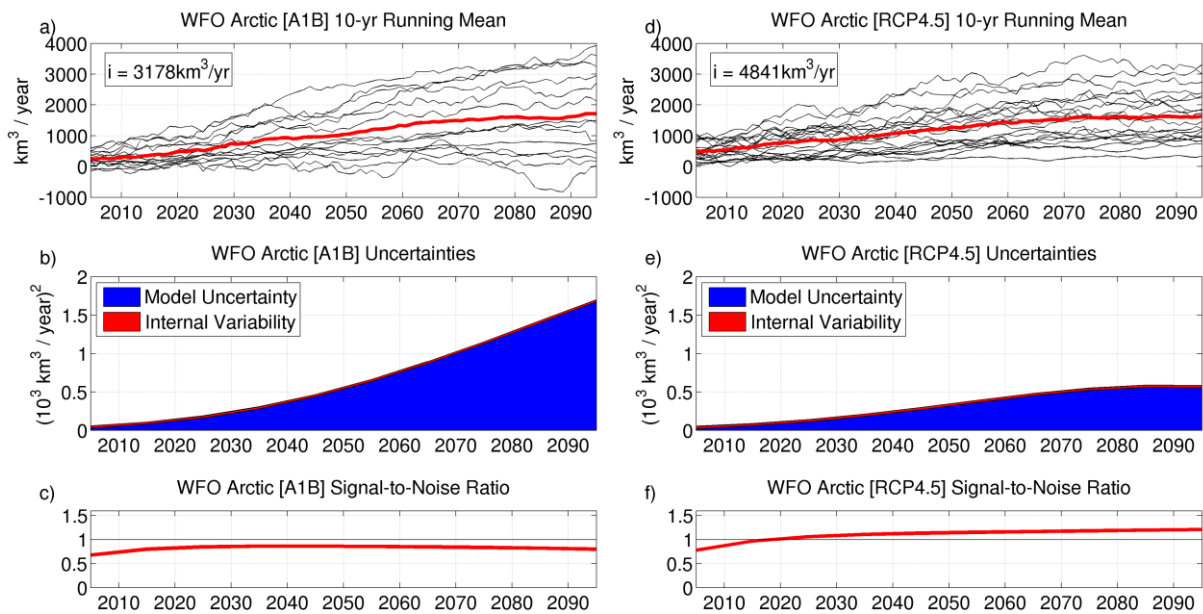




723

724 **Fig. 7** Uncertainties in the salinity projection for CMIP3 (**a-b**) and CMIP5 (**c-d**). (**a**) and (**c**):  
 725 the model uncertainties in the salinity projections. (**b**) and (**d**): signal-to-noise ratio with a 90%-  
 726 confidence limit (ratio of 1 is given by the black contour)

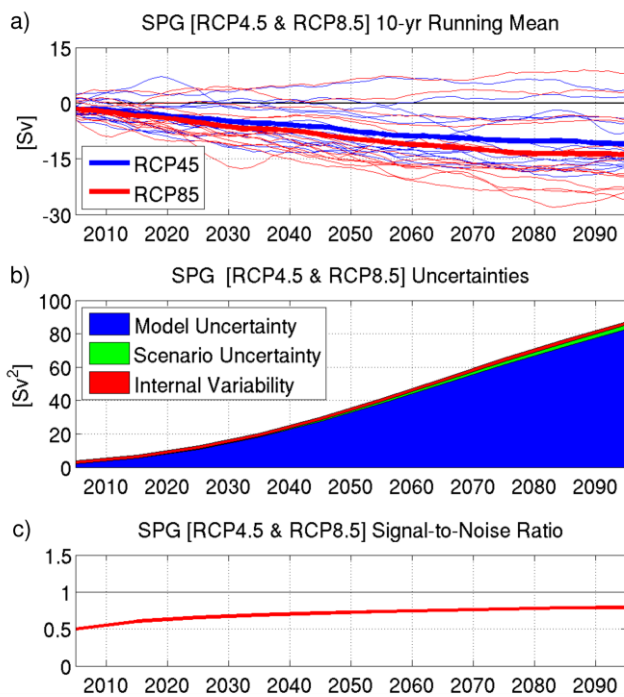
727



728

729 **Fig. 8** Sources of uncertainty in the projection of freshwater flux anomalies into the Arctic  
 730 Ocean for CMIP3 (a-c) and CMIP5 (d-f). (a) and (d): The individual model runs (black) and  
 731 the ensemble-mean (thick red). A 10-year running mean is applied. The climate mean for the  
 732 period 1970-2000 is removed. (b) and (e): absolute values of the model uncertainty and the  
 733 internal variability. (c) and (f): signal-to-noise ratio

734

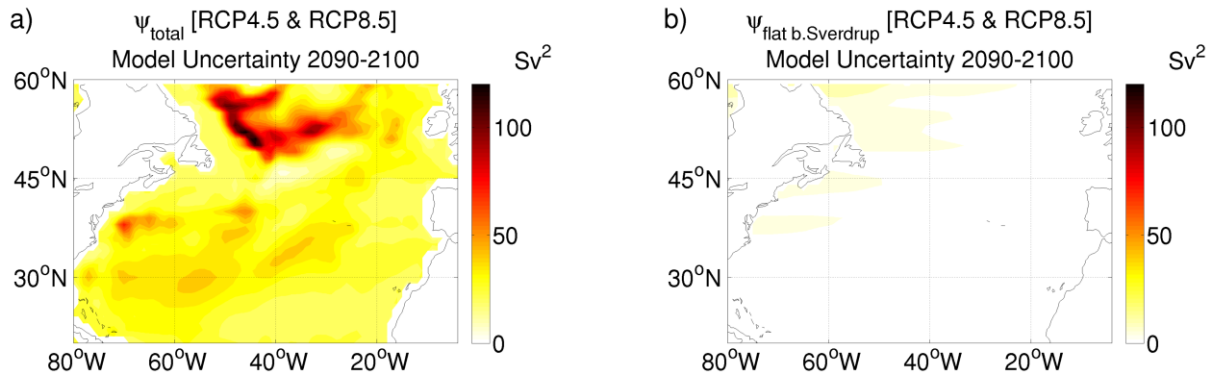


735

736 **Fig. 9** Sources of uncertainty in the subpolar gyre (SPG) index projection until 2100 in the  
 737 CMIP5 model ensemble using the scenarios RCP4.5 and RCP8.5. (a) SPG index long-term  
 738 changes of the individual models; only 10-year running mean is presented (the climate mean  
 739 has been removed); (b) individual absolute uncertainties of the SPG index projections; (c)  
 740 signal-to-noise ratio for the SPG index changes

741

742



743

744 **Fig. 10** Model uncertainty of the barotropic streamfunction projections of CMIP5 for 2090-  
 745 2100; (a) for the total barotropic streamfunction from the model output and (b) for the flat-  
 746 bottomed Sverdrup transport computed from wind stress data. The scenarios RCP4.5 and  
 747 RCP8.5 are used